Turbulence, Heat and Mass Transfer 8

Actuation of the flow field around a frontstep with a rounded leading edge

G. Minelli[1], S. Krajnović[1] and B. Basara[2]

[1]*Department of Applied Mechanics. Chalmers University of Technology, 412 96 Gothenburg, Sweden minelli@chalmers.se*

[2]*Advanced Simulation Technologies, AVL List GmbH, Hans-List-Platz 1, 8020 Graz, Austria*

Abstract — Large Eddy Simulations (LES) are conducted to study the actuated flow field around a bluff body. The model is a simplification of a section of a truck cabin. The aim is to model the separation of the flow acting at the front part, the so called A-pillar. LES data show the connection between orientation and frequency of the actuation in comparison with drag reduction and separation mechanism. The flow is post processed using modal and frequency decompositions. Relevant results in terms of drag coefficient reduction were observed for the actuated flow. An optimal actuation in terms of induced frequency and drag reduction is also found.

1. Introduction

Flow control can be defined as the manipulation of the flow field to a more desired state, by an imposed actuation. Generally, flow control methods can be classified as passive or active. Krajnović (2014) proved passive flow control to be effective in delaying flow separation but this methodology is not always adaptable due to the design constraints. The optimization of aerodynamic performances by means of Active Flow Control (AFC) has been proven to be extremely effective when applied to both aerodynamic (Amitay et al., 2001) and bluff bodies (Pastoor et al., 2008; Parkin et al., 2013). Reviews of these techniques and devices were provided by Gad-el Hak (1998) and, more recently, by Cattafesta and Sheplak (2011). The AFC can be classified into two main categories. The first consists of flow control by means of moving surfaces such as moving cylinders (Han and Krajnović, 2013). The second is based on introducing momentum into the flow by blowing and sucking air through orifices. Now, the traditional methodology of steady blowing and suction of air, used by Krajnović et al. (2010) and by Krajnović and Fernandes (2011), has been overtaken by the state of the art, temporary variant actuation. The latter technique uses a fraction of the power otherwise needed, and a Zero Net Mass Flux (ZNMF) of blown and sucked air. Promising results were found for several studies, both experimental (Amitay and Glezer, 2002) and numerical (You and Moin, 2008) for both airfoil (Amitay and Glezer, 2002; You and Moin, 2008) and bluff bodies (Brunn and Nitsche, 2006). A ZNMF jet is employed in this work to reduce the separation of the boundary layer from the surface of a bluff body. The separation of the flow that occurs at the trailing edge of a bluff body has been studied in different works, e.g. by Pastoor et al. (2008) and Parkin et al. (2013). Instead, the model used in this work imitates a truck cabin section and focuses on the separation acting at the front rounded corner, the so called A-pillar.

The numerical study is conducted with Large Eddy Simulations (LES) with the standard Smagorinsky Sub-Grid Scale (SGS) model in order to reproduce the unsteady actuation and resolve a large part of the unsteady structures that are present in the flow.

Understanding the flow separation mechanism and the interactions in separated flow regions is also challenging. A modal analysis is thus needed to extract the flow features. LES results were post-processed by means of POD by Östh et al. (2013); thus the modal decomposition

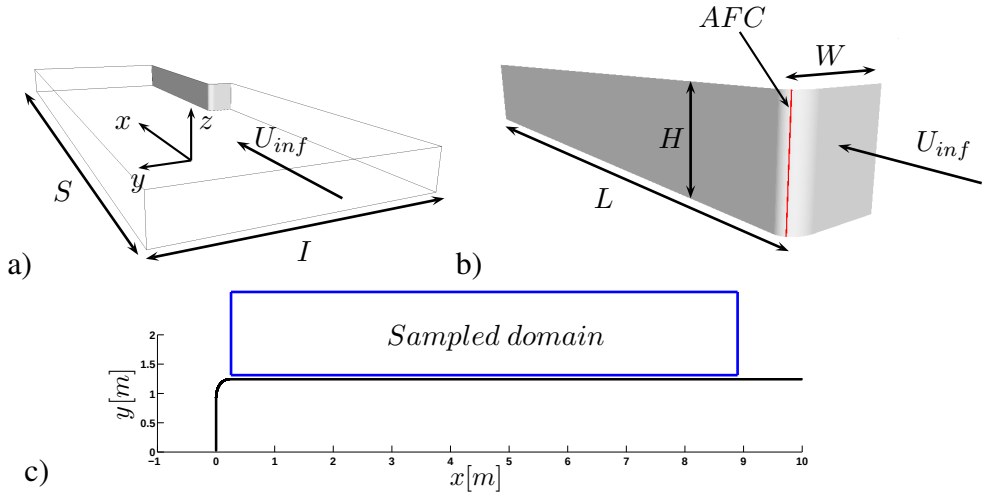

Figure 1: The computational domain, the model and the sampled plane.

mentioned was used in this work. A Fast Fourier Transform (FFT) analysis was also made to extract frequencies and characterize the flow's main structures found in the POD.

This paper is organized in three sections. The first part describes the computational case, the numerical details of the simulation and the description of the POD approach. An interpretation of the results is reported in the second part. The main results are summarized in the conclusions.

2. Numerical Set-up

The model is placed in a computational domain shown in Fig. 1a). The reference dimension of the section is, $W = 1.25m$, Fig. 1b). The model has a length of $L = 8W$, and a height of $H = 1.12W$. The length of the domain is $S = 19.2W$ and the width is $I = 8W$. A uniform and steady velocity, $U_{inf} = 0.64m/s$, is applied at the inlet. The resulting Reynolds number based on the double width of the section, $2W$, and U_{inf} is $Re = 1 \times 10^5$. A homogeneous Neumann boundary condition is applied at the outlet. The surfaces of the body are treated as no slip walls. Periodic boundary conditions are imposed at the upper and lower walls which define the height, H, of the section. Symmetry boundary conditions are set at the two side walls, which define the width, I, of the domain. A time varying velocity, $U_{AFC} = 0.1U_{inf}\sin(t2\pi f_a)$, is set at the actuation area highlighted in red in Fig. 1b). f_a is the chosen actuation frequency. All the frequencies in the present work are described in terms of Strouhal number (St), computed as $St = \frac{f_a 2W}{U_{inf}}$. A cut plane (Fig. 1c)) is sampled during the simulation to post-process the flow.

The governing LES equations are the spatially implicitly filtered Navier-Stokes equations, where the spatial filter is determined by the characteristic width $\Delta = (\Delta_1\Delta_2\Delta_3)^{\frac{1}{3}}$, and Δ_i is the computational cell size in the three coordinate directions.

$$\frac{\partial \bar{u}_i}{\partial t} + \frac{\partial}{\partial x_j}(\bar{u}_i\bar{u}_j) = -\frac{1}{\rho}\frac{\partial \bar{p}}{\partial x_i} + \nu\frac{\partial^2 \bar{u}_i}{\partial x_j \partial x_j} - \frac{\partial \tau_{ij}}{\partial x_j} \tag{1}$$

and

$$\frac{\partial \bar{u}_i}{\partial x_i} = 0. \tag{2}$$

Here, $\bar{u}_i$ and $\bar{p}_i$ are the resolved velocity and pressure, respectively, and the bar over the variable denotes the operation of filtering. The influence of the small scales in Eq. 1 appears in the SGS stress tensor, $\tau_{ij} = \overline{u_i u_j} - \bar{u}_i\bar{u}_j$. The algebraic eddy viscosity model, described by Smagorinsky

(1963), is employed in this work. The Smagorinsky model represents the anisotropic part of the SGS stress tensor, τ_{ij} as

$$\tau_{ij} - \frac{1}{3}\delta_{ij}\tau_{kk} = -2\nu_{sgs}\bar{S}_{ij} \tag{3}$$

where the SGS viscosity is

$$\nu_{sgs} = (C_s f \Delta)^2 |\bar{S}| \tag{4}$$

and,

$$\bar{S} = \sqrt{(2\bar{S}_{ij}\bar{S}_{ij})} \tag{5}$$

where

$$\bar{S}_{ij} = \frac{1}{2}\left(\frac{\partial \bar{u}_i}{\partial x_j} + \frac{\partial \bar{u}_j}{\partial x_i}\right) \tag{6}$$

The Smagorinsky constant, $C_s = 0.1$, previously used in bluff body LES by Krajnovic (2009), is used in the present work. f in the expression for the SGS viscosity is the Van Driest damping function.

$$f = 1 - exp\left(\frac{-n^+}{25}\right) \tag{7}$$

where n^+ is the wall normal distance in viscous units.

The simulations in this work are made with the commercial finite volume CFD solver, AVL FIRE (AVL 2010, 2010). AVL FIRE is based on the cell-centered finite volume approach. The grid topology is constructed using the O-grid technique in order to concentrate most of the computational cells close to the body. Figure 2 shows a cut plane of the grid employed and its refinement at the active flow control region. The grid resolution has an average value in the wall normal direction of $n^+ = 0.45$ and a maximum value of $n^+ = 1.7$. Here, $n^+ = \frac{u_\tau n}{\nu}$, with the friction velocity u_τ. The resolution in the spanwise direction is $\Delta l^+ < 30$, and the resolution in the streamwise direction is $\Delta s^+ < 100$. $\Delta l^+ = \frac{u_\tau \Delta l}{\nu}$ and $\Delta s^+ = \frac{u_\tau \Delta s}{\nu}$. The chosen time step, $\Delta t^* = \Delta t U_{inf}/2W$ is 1.28×10^{-3} for all the simulations, resulting in a CFL number lower than 1 in the entire domain. All the simulations were run first until the flow was fully developed. This was followed by an averaging of $t^* = tU_{inf}/2W = 25$.

2.1. Numerical accuracy

The numerical accuracy is ensured by performing the unactuated flow field simulation on a coarser grid. The number of computational cells of the coarse grid has been reduced by 35%. The coarsening procedure affects only the streamwise and spanwise directions and thus the grid has not been coarsened in the wall normal direction. Figure 3a) shows the streamwise velocity profiles of both the fine and the coarse grids. Figure 3b) shows the drag signal of the coarse and fine grid simulations. The mean value of C_d differs by 0.5%, and a good agreement between the measured profiles, Fig. 4a), confirms that mesh independence is achieved.

2.2. Modal and frequency analyses

One single POD temporal coefficient can oscillate at different frequencies, while the Fast Fourier transform (FFT) analysis represents the area of interest of the actual frequencies of the flow. It is interesting to compare the two approaches in order to gain a complete understanding of the flow structures in terms of both the energy content and characteristic frequencies.

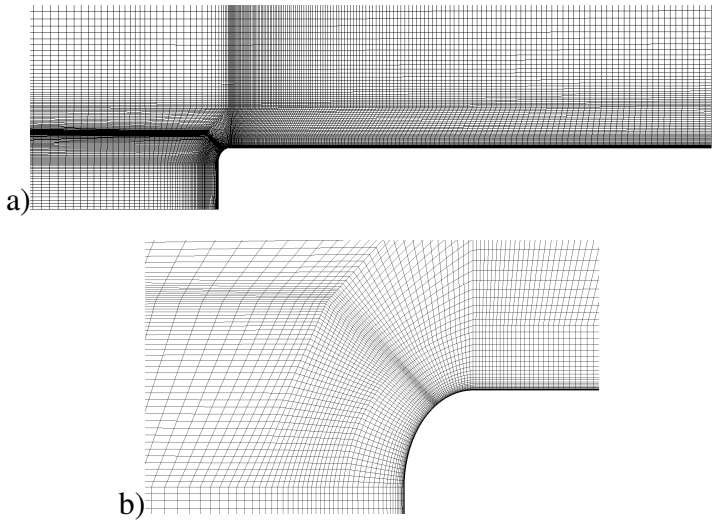

Figure 2: A top view of a plane cut of the computational grid.

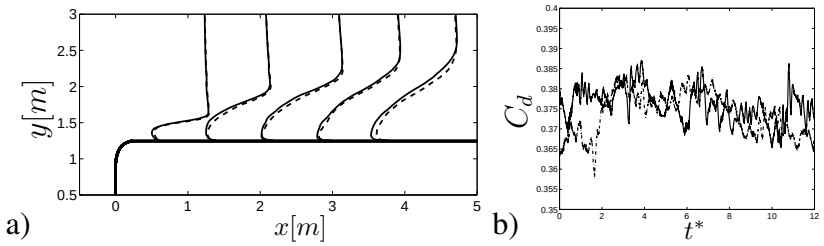

Figure 3: a) Averaged streamwise velocity component profiles. b) C_d over time. (------) coarse grid, (——) fine grid.

The present POD is made of a snapshot sequence of data V_1^N,

$$V_1^N = (v_1, ..., v_n) \in \mathbb{R}^{N_x \times N} \tag{8}$$

where the generic m_{th} snapshot is space and time dependent as,

$$v_m = v_m(x, t_m) \tag{9}$$

As it originally proposed by Lumley (1970), this method is based on an energy ranking of orthogonal structures computed from a correlation matrix of the snapshots used. A singular value decomposition approach is used to conduct the POD analysis on the matrix V_1^N as,

$$V_1^N = A\Sigma Q^T \tag{10}$$

Here, matrix A contains the spatial structures, and matrix Q contains the temporal structures. Matrix Σ contains the singular values that rank the energy content of each mode. In the present work, the POD study is performed over 1000 equispaced time steps and the non dimensional time step $\Delta t^\star$ between each snapshot is chosen as $\Delta t^\star = 1.28 \times 10^{-2}$.

A snapshot dependence study is performed to ensure the accuracy of the decompositions. Figure 4 compares the modes' energy content of three different decompositions. The fine decomposition is performed over 1000 equispaced snapshots, and the two coarser decompositions are performed over 800 and 600 snapshots, respectively. Figure 4 shows the non dependency of

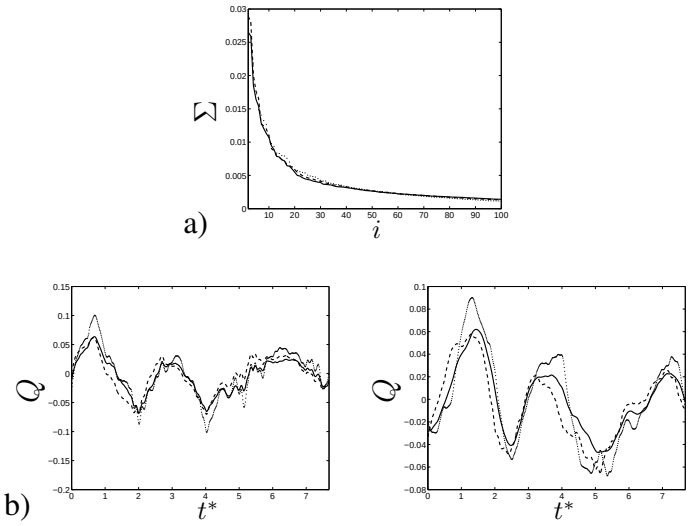

Figure 4: a) Pressure modes energy content (% of total energy) of three different decompositions, from mode 2 to mode 100. b) Second (left) and third (right) pressure temporal modes for three different decompositions. (——) 1000 snapshots, (------) 800 snapshots, $(\cdots\cdots)$ 600 snapshots.

the modal analysis from the number of snapshots. Reducing the number of snapshots by 40%, both the energy content of the first 100 modes' plot, Fig. 4a), and the time history of the first two temporal modes' plot, Fig. 4b), does not differ excessively from the POD results of the first set of snapshots.

3. Results

A preliminary study to evaluate the direction of the actuation and the accuracy of the POD is presented in the first part of this section. Results from both unactuated and actuated flows at different actuation frequencies are presented in the second part.

3.1. Preliminary study

Different directions of the actuation are tested in a preliminary study. The normal actuation with respect to the local direction of the flow, black arrow shown in Fig. 5a), is the most effective in terms of drag reduction, Fig. 5b). Thus the normal actuation was kept for all the actuated configurations.

The unactuated flow field was first studied to get a better understanding of its main features. The FFT analyses of the drag coefficient, shown in Fig. 6, highlights important frequencies in a range from $St = 0.23$ to $St = 8$. Thus, four different configurations are selected for the actuation: case 1 actuated at $St = 0.97$, case 2 at $St = 1.95$, case 3 at $St = 3.9$ and case 4 actuated at $St = 7.8$.

The POD performed on the unactuated flow is able to reproduce the main features of the flow. Figure 7 shows the energy content of the first 50 pressure modes with respect to the time interval considered. Mode 1 corresponds to the averaged flow field and is the mode that contains the most energy. Figure 7 shows that modes contain the same amount of energy in pairs. Each pair of modes, with the exclusion of mode 1, describes the characteristic travelling structures acting in the flow domain. Thus, mode 2 and 3 describe the most energetic travelling structures. Figure 8 depicts a reconstruction of the pressure field by characteristic modes in comparison with the

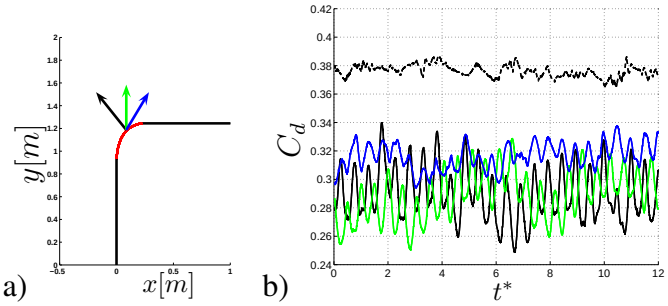

Figure 5: a) Three different actuation configurations. b) C_d over time. Unactuated flow (------), actuated at normal direction (——), actuated at 45 degrees (——) and actuated at 20 degrees (——), with respect to the unactuated flow direction

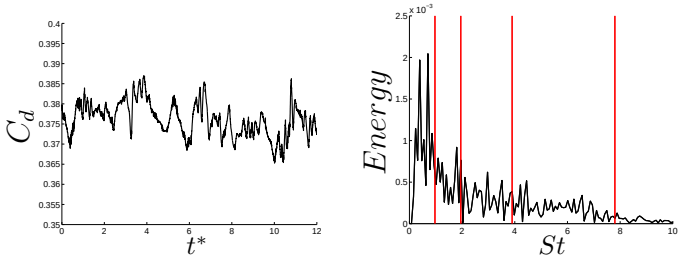

Figure 6: C_d of the unactuated flow (left) over time. FFT of C_d. The red lines represent the chosen actuation frequencies (right).

instantaneous pressure flow field, Fig. 8c). Both the small structures at the front and the larger structures at the back are captured by two different pairs of modes, Fig. 8a). In merging the modes, a reconstruction in both time and space of the flow structures is observed, Fig. 8b). An FFT analysis conducted on the same set of snapshots indicates the spatial distribution of the most important frequencies describing the flow field. FFT is applied to each cell of the sampled domain. Summing up the FFT from all cells results in the plot in Fig. 9a). This defines the most energetic frequency all over the domain. Figure 9a) shows the most energetic peak at $St = 0.47$. Figure 9b) shows the spatial distribution of two different frequencies. Figure 9 highlights the difference in energy content of the two frequencies considered. The frequency at $St = 0.47$ has a larger energy content and space distribution, while the frequency at $St = 1.88$ is only visible in a limited area and its energy is considerably lower. Figure 10 shows the PSD of the most energetic pressure temporal mode. This plot highlights the same peak as is shown in Fig. 9a), showing good agreement between POD and FFT analysis results.

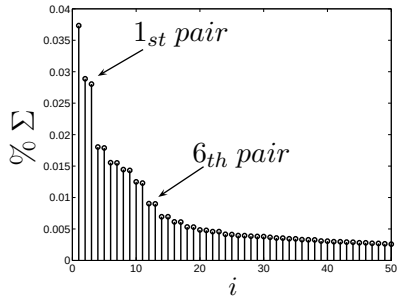

Figure 7: First 50 most energetic pressure modes.

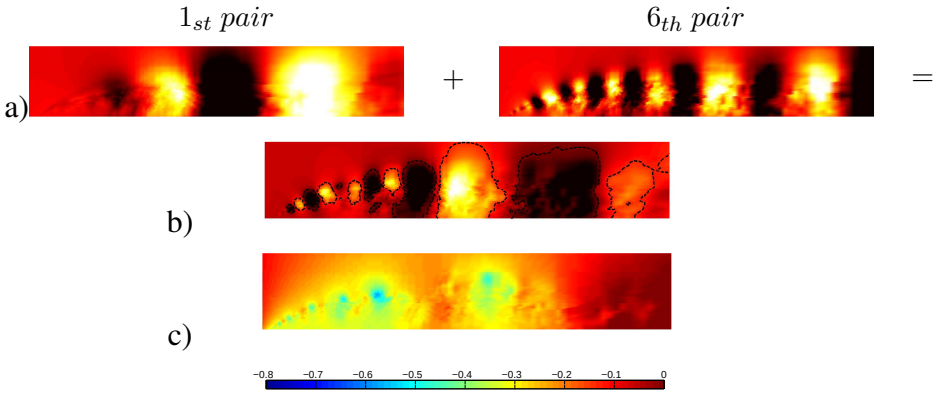

Figure 8: a)Spatial distribution of the first and sixth pair of modes' travelling structures. b) A reconstruction of the pressure field using the first and sixth pair of modes. c) A snapshot of the relative pressure flow field, in [Pa].

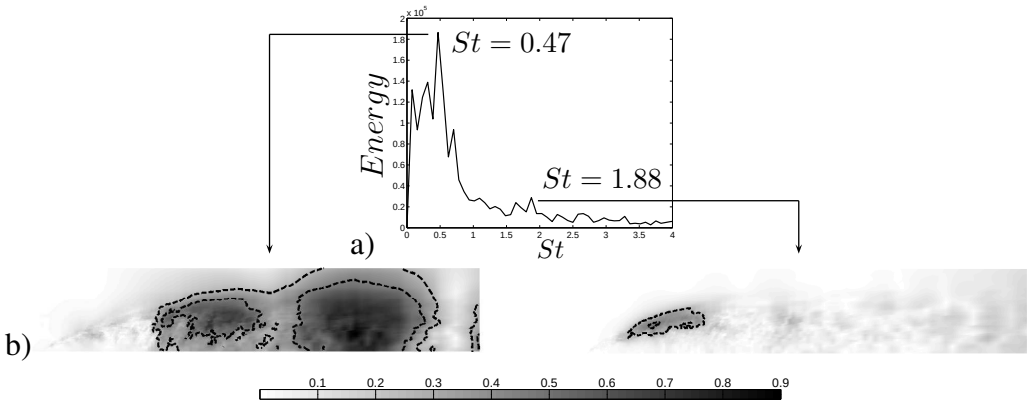

Figure 9: FFT analysis on the sampled domain.

3.2. The actuated flow

An optimal actuation is found in terms of induced frequency and drag reduction. The actuation introduces artificial oscillations in the flow, visible from the Root Mean Square (RMS) values of the drag, Table 1. The maximum drag reduction and minimum induced oscillations are observed for case 3, Table 1. Nevertheless, a deeper study of the instantaneous flow field is needed to gain a better understanding of the mechanisms that lead to the optimal or non optimal configurations. Figure 11 shows how the actuation frequency affects the flow around the body. Figure 11a) shows the spatial distribution of the actuation frequency for each case, respectively. The area characterized by the actuation frequency decreases, increasing the actuation frequency. As described for Fig. 9, Fig. 11b) shows the sum of the Power Spectral Density (PSD) for all cells of the sampled domain. The first two cases show a clear peak defined by the actuation frequency. The energy of the actuation decreases for case 3 with respect to the natural frequencies of the flow; a broader spectra defines that the actuation frequency is not clearly dominant. The POD results in Fig. 12 show the same results as are observed in Fig. 11. Increasing the actuation frequency, the first most energetic mode decreases its area of interest, Fig. 12b), and its energy content in comparison to the other modes, Fig. 12a). Figure 12c) shows the orbit plot of the most energetic mode for cases 1, 2 and 3. This plot describes the time distribution of the POD's modes and highlights their possible periodicities. All cases present a strong periodicity that is

Figure 10: POD most energetic pressure mode (left), PSD of the most energetic pressure temporal mode (right).

Table 1: Mean C_d and its Root Mean Square values.

Case	C_d	$C_d\ RMS$
Unactuated flow	0.38	0.004
1. Actuated flow at $St = 0.97$	0.33	0.024
2. Actuated flow at $St = 1.95$	0.29	0.018
3. Actuated flow at $St = 3.9$	0.25	0.009
4. Actuated flow at $St = 7.8$	0.30	0.024

represented by the actuation frequency.

The signal of the coefficient of drag, C_d, depicts the trend of the drag increasing the actuation frequency. Figure 13 shows C_d and its PSD for four different actuated cases. As was mentioned before, an optimal frequency is found and shown in Fig. 13. The increase in the actuation frequency does not always benefit the aerodynamic performance of the model. In particular, case 4 shows an increase in both the induced fluctuation and mean value of the drag. Figure 13b) shows how the induced fluctuation has less energy as compared to the natural fluctuations of the flow. As was observed in Fig. 11b), a broader spectrum of characteristic frequencies is visible in Fig. 13b) case 3, while all the other cases present a distinct peak at the actuation frequency. Figure 14 shows a zoom of the coefficient of drag in comparison with the sinusoidal actuation signal. Figure 14 clearly shows the difference in the dependency of the drag from the actuation. C_d of cases 1 and 4 shows a strong dependence from the actuation. C_d of case 2, and especially

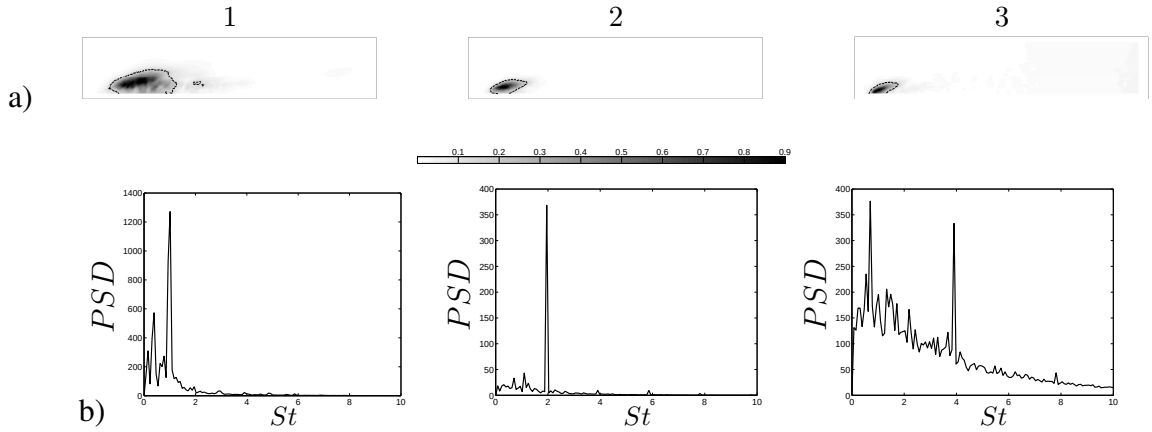

Figure 11: a) Spatial distribution of the energy of the actuation frequency for each case. b) Sum of the PSD of all cells all over the sampled domain. From left to right, case 1, case 2 and case 3.

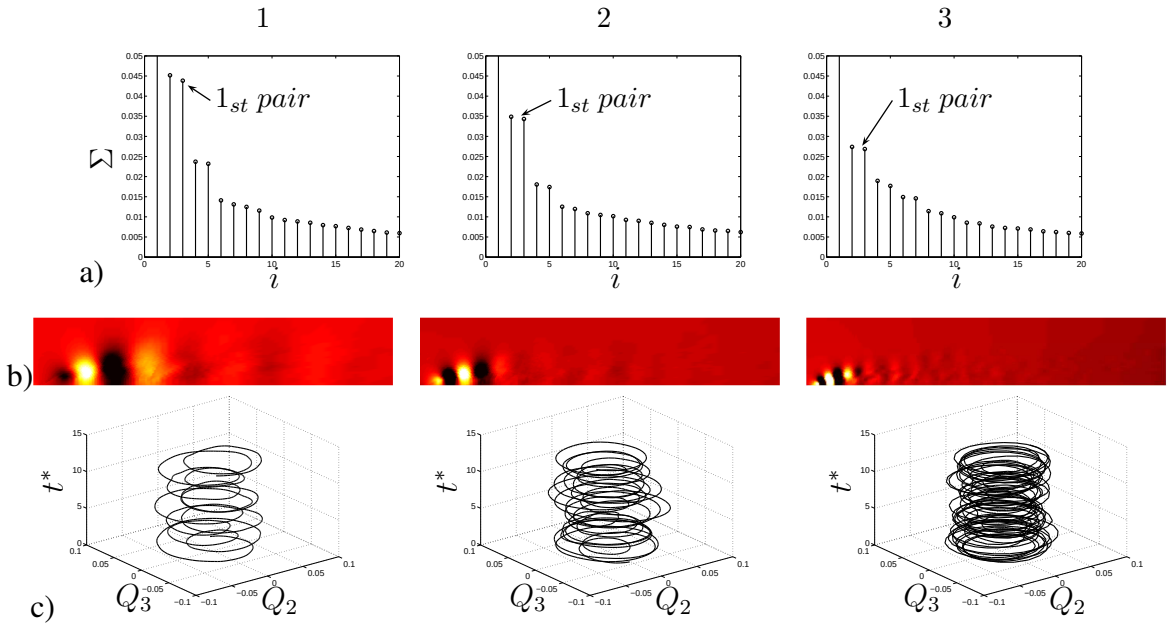

Figure 12: a) Energy content of the first 20 pressure modes. b) Spatial distribution of the most energetic mode. c) Orbit plot of the first most energetic mode. From left to right, case 1, case 2 and case 3

case 3, shows a weaker dependence from the actuation. In the latter case, the actuation is not able to force the drag signal following its oscillations, benefitting the overall performance. Figure 15 shows the instantaneous pressure field for the four different configurations. The low pressure areas at the front part indicate the cores of the Kelvin-Helmotz vortices that arise after the separation at the rounded corner. All V_{afci} are forced by the actuation that defines their frequency, position and dimension. Cases 1 and 2 present larger vortex cores. In these configurations, the vortex has time to develop, between a period and its subsequent, larger structures that arise, V_{afc1} and V_{afc2}. The first three cases present a definite trend; increasing the frequency, the dimension of V_{afci} decreases and the vortex remains more attached to the surface of the body. Case 4 eludes from the described path; the higher momentum that is introduced gives more energy to the vortices V_{afc4}, which separate from the surface of the model and shape the larger structures, V_{k4}, responsible for the increase in the drag's mean value. In this case, large oscillations, comparable with the first case, are visible in the C_d signal. Comparing the nature of the introduced oscillations, in the first case they are introduced by the large actuation period that allows V_{afc1} to separate and develop periodically. The core of V_{afc1} remains close to the surface of the model, yet being large. In case 4 instead, the high momentum that is introduced forces the flow to separate and reattach at the actuation spot, characterizing the drag oscillations. V_{afc4} is smaller than V_{afc1} but at the same time more distant from the surface. This fact allows the formation of a new and larger vortex, V_{k4}, that characterizes the mean value of the drag, widening the recirculation bubble, Fig. 16. Both instantaneous and averaged streamwise velocity flow fields are presented in Fig. 16. The reduction of the recirculation bubble is clearly in favour of configuration 3. Configuration 4 in Fig. 16, confirms the presence of an optimal actuation. Indeed, Fig. 17 describes the trend of the flow behaviour increasing the actuation frequency. The actuation frequency is increased from case 1 to 4, (blue line in Fig. 17), but both C_d and RMS trend plots show a minimum for case 3. In particular, a drag reduction of 34% in comparison with the unactuated case is observed in case 3. The fluctuations induced by actuation 3 decrease by 62% in comparison with the drag fluctuations of case 1.

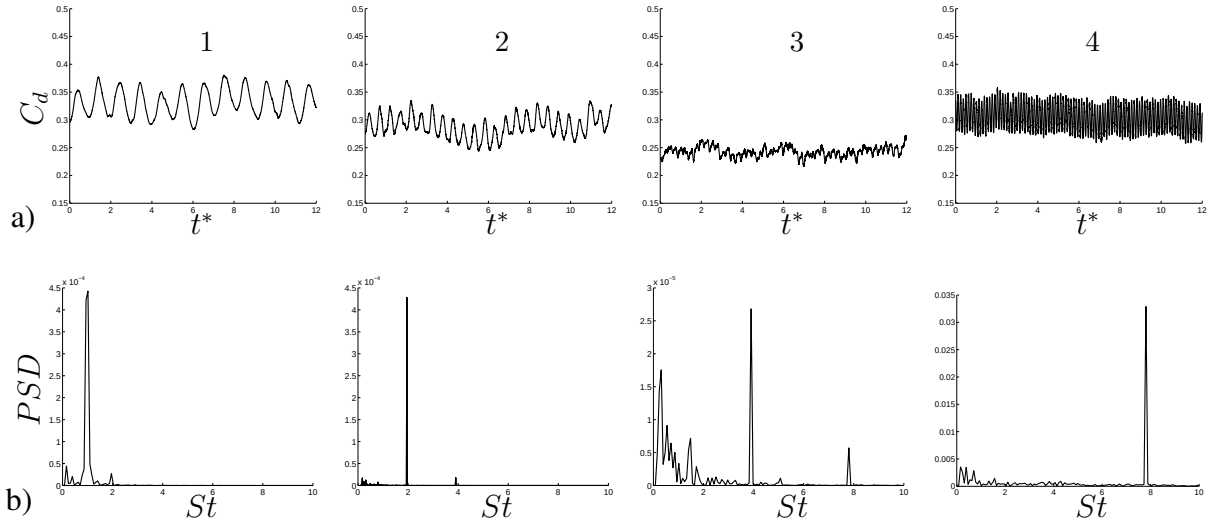

Figure 13: a) C_d time history. b) PSD of C_d. From left to right, case 1, 2, 3 and 4.

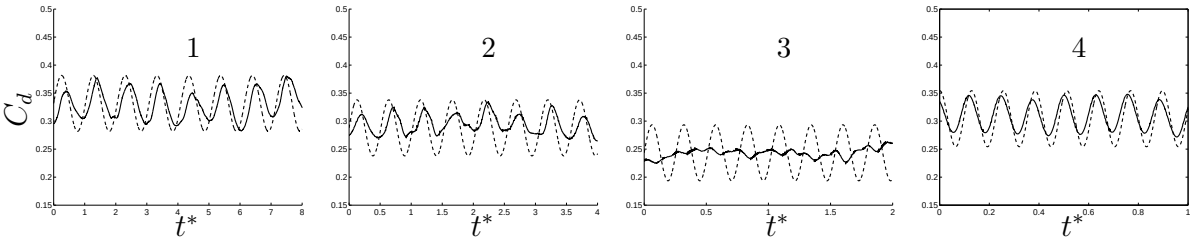

Figure 14: C_d (——) and the actuation signal (------) over time. From left to right, case 1, 2, 3 and 4.

4. Conclusion

LES at $Re = 1 \times 10^5$ were conducted to analyse the actuation of the flow field around a rounded leading edge frontstep that represents a simplified section of a truck cabin. Different configurations of the actuation were tested. A preliminary study shows that the actuation is most efficient when the blown and sucked air from the orifice is perpendicular to the local direction of the flow. Thus the perpendicular configuration is kept to conduct the study at different actuation frequencies. The modal decomposition and the frequency analysis were used to define the range of frequencies that describes the flow field and to extrapolate its main characteristics. Four actuation frequencies were chosen to study the effects of the control on drag reduction and induced actuation. The instantaneous and averaged pressure and velocity fields are studied to get a better understanding of the separation mechanism at the rounded corner subjected to different actuations. It was furthermore found that, the aerodynamic performances are strongly affected by the actuation, and the study shows the presence of an optimal configuration found in the case actuated at $St = 3.9$. Case 4 diverts from the performance trend of the previous cases, giving interesting results on the separation features. The dependency of the drag from the actuation frequency plays a crucial role in finding the optimal configuration. The overall aerodynamic performance of the model benefits when the drag signal becomes independent from the actuation. Both RMS and the mean value of the drag coefficient show a minimum at the optimal configuration. In particular, a drag reduction of 34% is observed in case 3.

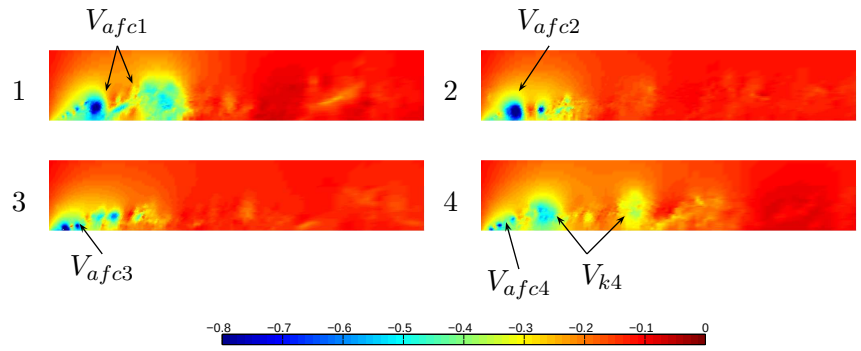

Figure 15: Instantaneous relative pressure field for each actuated configuration, in [Pa].

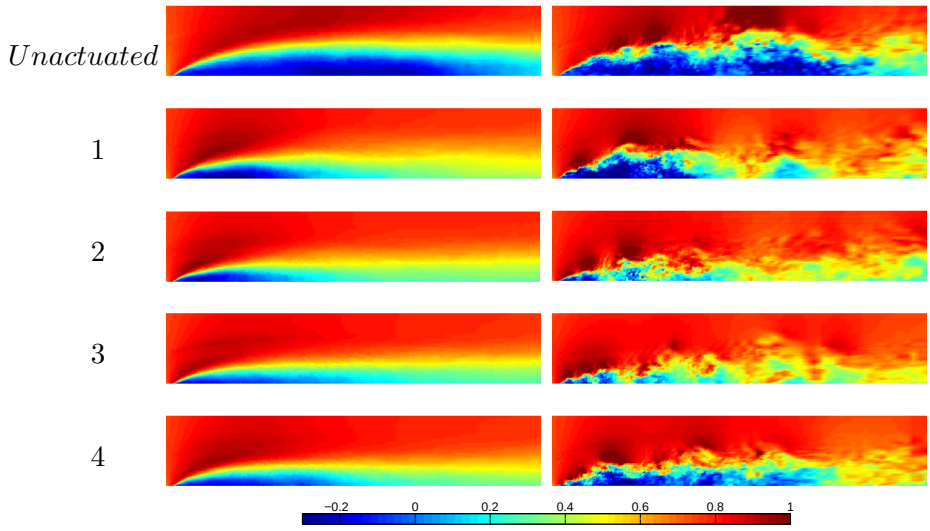

Figure 16: Recirculation bubble reduction. Instantaneous streamwise velocity component (left) and averaged streamwise velocity component (right), in [m/s].

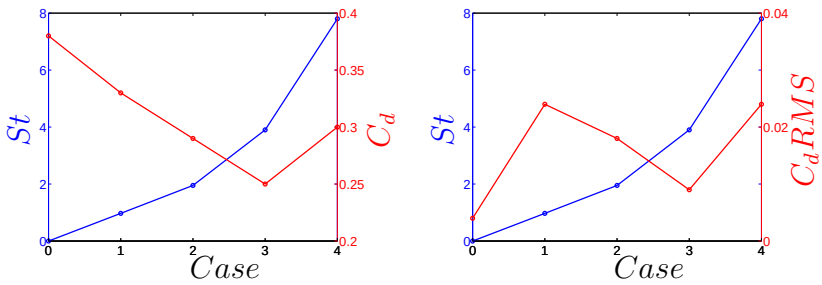

Figure 17: C_d and its RMS trends (——) with increasing actuation fequency (——).

Acknowledgements

This work is supported financially by the Swedish Energy Agency. Software licenses were provided by AVL List GMBH. Computations were performed at SNIC (Swedish National Infrastructure for Computing) at the Center for Scientific Computing at Chalmers (C3SE) and the National Supercomputer Center (NSC) at LiU.

References

M. Amitay and A. Glezer. Role of Actuation Frequency in Controlled Flow Reattachment over a Stalled Airfoil. *AIAA Journal*, 40(2):209–216, Feb. 2002.

M. Amitay, D. E. Parekh, D. R. Smith, V. Kibens, and A. Glezer. Aerodynamic flow control over an unconventional airfoil using synthetic jet actuators. *AIAA Journal*, 39(3):361–370, 2001.

AVL 2010. AVL Fire manual, v2010. Edition 11, 2010.

A. Brunn and W. Nitsche. Active control of turbulent separated flows over slanted surfaces. *International Journal of Heat and Fluid Flow*, 27(5):748–755, Oct. 2006.

L. N. Cattafesta and M. Sheplak. Actuators for Active Flow Control. *Annual Review of Fluid Mechanics*, 43(1):247–272, Jan. 2011.

M. Gad-el Hak. Introduction to flow control. *Flow Control*, (1904):1–107, 1998.

X. Han and S. Krajnović. Large Eddy Simulation of Flow Control Around a Cube Subjected to Momentum Injection. *Journal of Fluid Mechanics*, 729(1-2):151–179, Apr. 2013.

S. Krajnovic. Large eddy simulation of flows around ground vehicles and other bluff bodies. *Philosophical transactions. Series A, Mathematical, physical, and engineering sciences*, 367 (1899):2917–2930, July 2009.

S. Krajnović. Large Eddy Simulation Exploration of Passive Flow Control Around an Ahmed Body. *Journal of Fluids Engineering*, 136(12):121103, Sept. 2014.

S. Krajnović and J. a. Fernandes. Numerical simulation of the flow around a simplified vehicle model with active flow control. *International Journal of Heat and Fluid Flow*, 32(1):192–200, Feb. 2011.

S. Krajnović, J. Östh, and B. Basara. LES study of breakdown control of A-pillar vortex. *International Journal of Flow Control*, 2(4):237–258, Dec. 2010.

J. L. Lumley. *Stochastic Tools in Turbulence SE - Applied Mathematics and Mechanics*, volume 12. Academic Press, New York, 1970.

J. Östh, B. R. Noack, S. Krajnović, D. Barros, and J. Borée. On the need for a nonlinear subscale turbulence term in POD models as exemplified for a high Reynolds number flow over an Ahmed body. *Journal of Fluid Mechanics*, pages 1–26, Oct. 2013.

D. J. Parkin, M. C. Thompson, and J. Sheridan. Numerical analysis of bluff body wakes under periodic open-loop control. *Journal of Fluid Mechanics*, 739:94–123, Dec. 2013.

M. Pastoor, L. Henning, B. R. Noack, R. King, and G. Tadmor. Feedback shear layer control for bluff body drag reduction. *Journal of Fluid Mechanics*, 608:161–196, 2008.

J. Smagorinsky. General circulation experiments with the primitive equations. *Monthly weather review*, 91 (3):99–165, 1963.

D. You and P. Moin. Active control of flow separation over an airfoil using synthetic jets. *Journal of Fluids and Structures*, 24(8):1349–1357, Nov. 2008.